Molecular Machines

International Edition: DOI: 10.1002/anie.201913798
German Edition: DOI: 10.1002/ange.201913798

Active and Unidirectional Acceleration of Biaryl Rotation by a Molecular Motor**

*Edgar Uhl, Peter Mayer, and Henry Dube**

Dedicated to Dr. Klaus Römer on the occasion of his 80th birthday

Abstract: *Light-driven molecular motors possess immense potential as central driving units for future nanotechnology. Integration into larger molecular setups and transduction of their mechanical motions represents the current frontier of research. Herein we report on an integrated molecular machine setup allowing the transmission of potential energy from a motor unit onto a remote receiving entity. The setup consists of a motor unit connected covalently to a distant and sterically encumbered biaryl receiver. By action of the motor unit, single-bond rotation of the receiver is strongly accelerated and forced to proceed unidirectionally. The transmitted potential energy is directly measured as the extent to which energy degeneration is lifted in the thermal atropisomerization of this biaryl. Energy degeneracy is reduced by more than 1.5 kcal mol^{-1}, and rate accelerations of several orders of magnitude in terms of the rate constants are achieved.*

Introduction

Molecular motors[1] allow the transformation of energy input at the molecular scale into directional motions and are thus envisioned to provide archetypal powering engines for future complex nanomachinery.[2] To date a variety of molecular setups have been made available that deliver such powered directional motions,[1a–m] and first attempts have been made to transmit their motions at the molecular scale[3] or integrate them into larger structures to perform macroscopic work.[4] However, at present, there is only limited knowledge about the actual amount of work that a single molecular motor can actively (against strain) perform, and thus critical information for the next leap in applicability is missing.[2b,5] A different yet related pressing issue is the question as to how the integration of a molecular motor unit into a larger structure can be achieved such that its directional motion is effectively translated into a potential energy increase at remote sites. Here we present a molecular machine setup **1** that allows for the first time the effective transmission of potential energy increases from a powering motor unit onto a remote receiver unit, which thus actively accelerates the motion of the latter (Figure 1).[6] We used an axially chiral biaryl as the receiver unit, which in its non-tethered form (reference compound **2**) undergoes slow and nondirectional atropisomerization rotation towards a 1:1 equilibrium of enantiomers (Figure 1 a). Coupling of a molecular motor unit enables us to drive this atropisomerization unidirectionally away from equilibrium. In contrast to an earlier reported system[3a] we have now shifted the rate-determining step of the machine's operation cycle from the motor helix inversion step to the atropisomerization of the remote biaryl (see the Supporting Information for a direct comparison of both systems). As a result, the biaryl atropisomerization is not passively following motor operation anymore but represents an energy hurdle against which the motor has to work actively. In machine **1**, a rate acceleration of several orders of magnitude for the biaryl atropisomerization was achieved by action of the motor, overpowering the intrinsic barriers for the isolated biaryl rotation (i.e., in model system **2** shown in Figure 1 b, c). With this molecular setup, critical design principles for advanced nanomachinery are unraveled, paving the way for the effective generation and precise transmission of potential energy at the smallest scales.

Results and Discussion

Molecular setup **1** incorporates a molecular motor unit that is based on the parent hemithioindigo (HTI) dye[7] (Figure 1). HTI belongs to the class of indigoid chromophores,[8] which are currently emerging as highly promising visible-light-responsive photoswitches.[9] The motor unit is connected covalently to a remote biaryl axis similar to an earlier described system that first evidenced the transmission of directional rotation from a molecular motor to a different molecular entity.[3a] In the herein presented setup **1**, a sterically strongly encumbered biaryl axis is introduced, which does not move in concert with the motor rotation. Different to the earlier four-state system that is governed only by the motor rotation steps, additional steps are introduced giving rise to an overall unidirectional six-step system (Figure 2). The six isomeric states are termed $\mathbf{A_T}$ for the tense state of **A**, $\mathbf{A_R}$ for the relaxed state of **A**, and correspondingly $\mathbf{B_R}$, $\mathbf{C_T}$, $\mathbf{C_R}$, and $\mathbf{D_R}$ for simplicity; their exact stereochemical assignments are

[*] M. Sc. E. Uhl, Dr. P. Mayer, Dr. H. Dube
Ludwig-Maximilians-Universität München
Department of Chemistry and Center for Integrated Protein Science CIPSM
Butenandtstr. 5–13, 81377 München (Germany)
E-mail: henry.dube@cup.uni-muenchen.de

[**] A previous version of this manuscript has been deposited on a preprint server (https://doi.org/10.26434/chemrxiv.10048871.v1).

Supporting information and the ORCID identification number(s) for the author(s) of this article can be found under: https://doi.org/10.1002/anie.201913798.

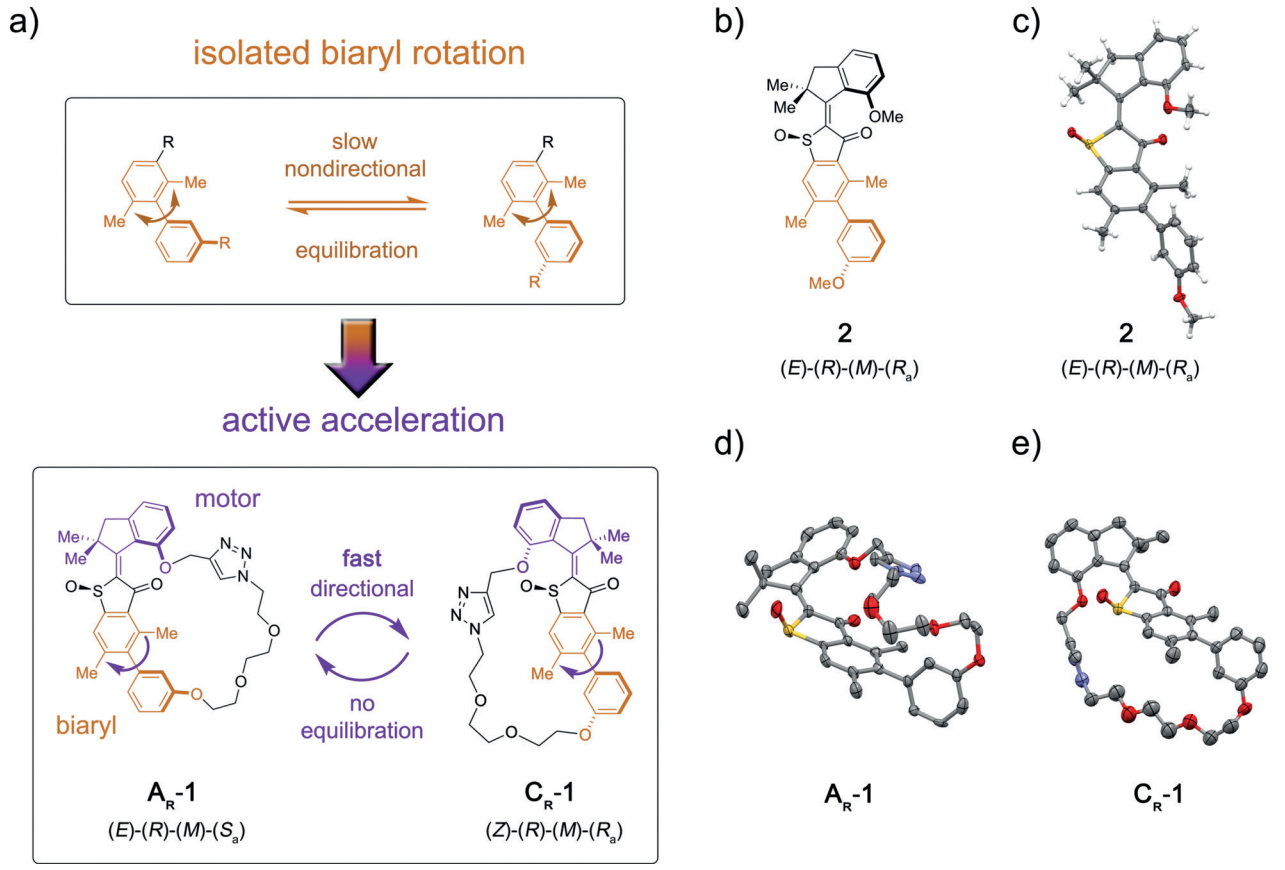

Figure 1. Integrated nanomachine **1** for potential energy transfer and active rate acceleration of biaryl rotation. a) Biaryl rotation can be slowed down by increased steric hindrance through introduction of two *ortho*-methyl groups. Atropisomerization proceeds nondirectionally towards a 1:1 equilibrium. In the integrated nanomachine **1**, biaryl rotation is accelerated, proceeds directional, and is not reaching a 1:1 equilibrium. b) Molecular structure of biaryl **2** serving as reference compound to determine the inherent biaryl atropisomerization rate. c) Molecular structure of **2** in the crystalline state. d) Structure of $\mathbf{A_R}$-**1** in the crystalline state. e) Structure of $\mathbf{C_R}$-**1** in the crystalline state. Structures in the crystalline state were determined from racemic materials; only the *R*-configured enantiomers are shown for clarity.[11]

given in Figure 1 and 2. Five of these steps can be observed directly experimentally, which also unequivocally confirms the existence of the sixth step and thus full directionality for the whole coupled 360° rotation of both the motor and the biaryl unit.

Motor system **1** was synthesized in a convergent fashion from a brominated HTI precursor to which the covalent tether containing a boronic ester function was attached by a copper-catalyzed click reaction. Afterwards a Suzuki-type cross-coupling reaction furnished macrocyclization, which was followed by oxidation to give the final structure **1**. The synthesis of model system **2** is described in the Supporting Information. For the two most stable states $\mathbf{A_R}$ (*E*-configured double bond) and $\mathbf{C_R}$ (*Z*-configured double bond) of **1** and for the stable *E*-isomeric state of **2**, crystals suitable for structural analysis were obtained (the *R*-configured isomers of racemic $\mathbf{A_R}$ and $\mathbf{C_R}$ are shown in Figure 1 d, e, respectively). The latter allowed us to directly assign the corresponding NMR spectra to specific molecular structures in solution. The conformations of the two most stable states in solution were further analyzed by NMR spectroscopy, which confirmed their close similarity to the crystalline state. The only notable difference is the apparent presence of a minor isomer species, which is in equilibrium with $\mathbf{A_R}$ at ambient temperature in solution. A comprehensive spectroscopic analysis (see e.g. the ECD spectra in Figure 3 a–d and Figures S17–S19 and S50 in the Supporting Information for full details) revealed this species to be the $\mathbf{A_T}$ isomer, possessing the same motor unit conformation but an atropisomerized biaryl axis as compared to $\mathbf{A_R}$. Variable-temperature assessment of the thermal equilibrium mixture allowed us to determine a free enthalpy difference $\Delta G = 1.41$–$1.30\ \mathrm{kcal\,mol^{-1}}$ (0 °C to 35 °C) between the two states involved using the Gibbs–Helmholtz equation.

As $\mathbf{A_R}$/$\mathbf{A_T}$ and $\mathbf{C_R}$ could be separated by HPLC, their behavior upon heating and irradiation at different temperatures could be scrutinized independently. Upon heating a solution of racemic $\mathbf{C_R}$ in $(CDCl_2)_2$ to 80 °C and up to 140 °C, the more stable $\mathbf{A_R}$ was formed in up to 93 %. This establishes a free enthalpy difference of $\Delta G = 1.7\ \mathrm{kcal\,mol^{-1}}$ in this temperature range between these two states. The corresponding kinetic analysis revealed a high energy barrier of $28.4\ \mathrm{kcal\,mol^{-1}}$ at 80 °C accompanying the thermal *Z*/*E* double bond isomerization. Upon cooling pure $\mathbf{C_R}$ down to −105 °C in CD_2Cl_2/CS_2 (4:1) and in situ irradiating the solution with 450 nm light at this temperature, a new set of

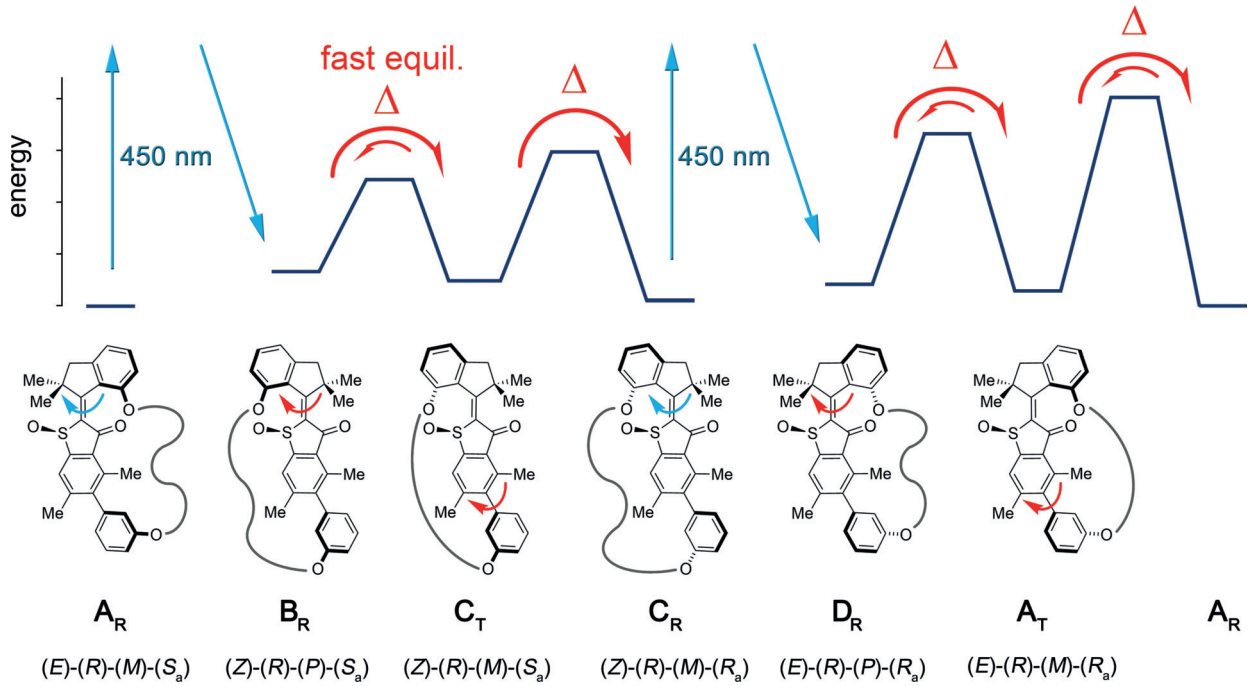

Figure 2. Qualitative ground-state energy profile of motor system **1**. Six states with different stereochemical configurations are populated during one full unidirectional 360° rotation. The covalent linkage between the motor and biaryl units is shown schematically for clarity reasons. The enantiomer of **1** with the *R*-configured sulfoxide stereocenter is shown dictating counterclockwise rotation of the motor as indicated by red and blue arrows.

signals emerged, which is different to the known signal set of $\mathbf{A_R}$ and $\mathbf{A_T}$ (Figure 3e). This new set of signals could be assigned to isomer $\mathbf{D_R}$ by NMR and ECD spectroscopy at low temperatures, which confirmed the *E* configuration of the double bond, the tilt of the biaryl unit, and a helix inversion of the motor unit (for detailed analysis, see Figure 3 and the Supporting Information). The $\mathbf{D_R}$ isomer signals decay to 75% within 28 min at −80°C in the dark while at the same time only the signals of the $\mathbf{A_T}$ isomer are growing to the same extent (Figure 3e). Again a thermal equilibrium between $\mathbf{D_R}$ (12% remaining) and $\mathbf{A_T}$ (88%) is observed at −60°C, which translates into a free enthalpy difference of $\Delta G = 0.84$ kcal mol^{-1} between the two states. Kinetic analysis of the thermal decay revealed an accompanying free activation enthalpy of $\Delta^{\ddagger}G = 13.9$ kcal mol^{-1} at −80°C for this process. At −40 to 0°C, decay of the $\mathbf{A_T}$ signals and concomitant growth of the known signals of $\mathbf{A_R}$ was observed until their equilibrium was reached (see the Supporting Information). Kinetic analysis of this process gave an associated free activation enthalpy of $\Delta^{\ddagger}G = 18.4$–$19.3$ kcal mol^{-1} at −40 to 0°C. Thus it was established that irradiation of pure *Z*-configured $\mathbf{C_R}$ leads to a first photoisomerization product $\mathbf{D_R}$, which thermally converts into the $\mathbf{A_T}$ isomer through a sole helix inversion at the motor unit. Unlike $\mathbf{D_R}$, the $\mathbf{A_T}$ isomer possesses a spring-loaded covalent tether between the rotor fragment and the biaryl unit owing to their large distance in this state. As a consequence, the $\mathbf{D_R}$ isomer does not completely decay, and an equilibrium concentration is established with this state still being populated. At slightly more elevated temperatures, $\mathbf{A_T}$ decays further by atropisomerization of its biaryl axis, thus eliminating strain in the tether.

Upon cooling the equilibrium solution of $\mathbf{A_R}/\mathbf{A_T}$ in CD_2Cl_2/CS_2 (4:1) to −105°C and irradiating in situ with 450 nm light inside the NMR spectrometer, the photoreaction of $\mathbf{A_R}$ was observed predominantly owing to its significantly larger abundance. A new set of signals emerged, which was different to the known signal set of $\mathbf{C_R}$ (Figure 3f). This set of signals was assigned to a rapidly interconverting mixture of $\mathbf{B_R}$ and $\mathbf{C_T}$ isomers based on NMR and ECD spectroscopy and the behavior of this set of signals under irradiation at very low temperature (see below). The observation of this new set of signals as the apparent photoproduct of $\mathbf{A_R}$ therefore directly confirms the expected photoisomerization directionality from $\mathbf{A_R}$ to $\mathbf{B_R}$, which then stabilizes itself further by undergoing fast helix inversion to $\mathbf{C_T}$ even at the low temperature.

At −80°C, the signals of $\mathbf{B_R}/\mathbf{C_T}$ decay almost completely in the dark while at the same time only the signals of $\mathbf{C_R}$ are growing to the same extent (Figure 3f). This gives a lower limit for the energy difference between $\mathbf{C_T}$ and $\mathbf{C_R}$ of 0.98 kcal mol^{-1} at this temperature under the conservative assumption that 5% residual $\mathbf{B_R}/\mathbf{C_T}$ are not detectable by NMR spectroscopy. Kinetic analysis gave a free activation enthalpy of $\Delta^{\ddagger}G = 13.4$–$13.7$ kcal mol^{-1} for the conversion of $\mathbf{C_T}$ into $\mathbf{C_R}$ at −100 to −75°C. Compared to the corresponding atropisomerization reaction of $\mathbf{A_T}$ to $\mathbf{A_R}$ ($\Delta^{\ddagger}G = 18.4$ kcal mol^{-1} at −40°C), the atropisomerization activation energy for the $\mathbf{C_T}$ into $\mathbf{C_R}$ conversion is significantly reduced. This experimental result can in part be attributed to the stronger strain in $\mathbf{C_T}$ than in $\mathbf{A_T}$, which is clearly evidenced by the presence of a thermal equilibrium between $\mathbf{A_R}$ and $\mathbf{A_T}$ while such an equilibrium is not present between $\mathbf{C_R}$ and $\mathbf{C_T}$. As a consequence, $\mathbf{C_T}$ lies considerably higher in energy than $\mathbf{A_T}$,

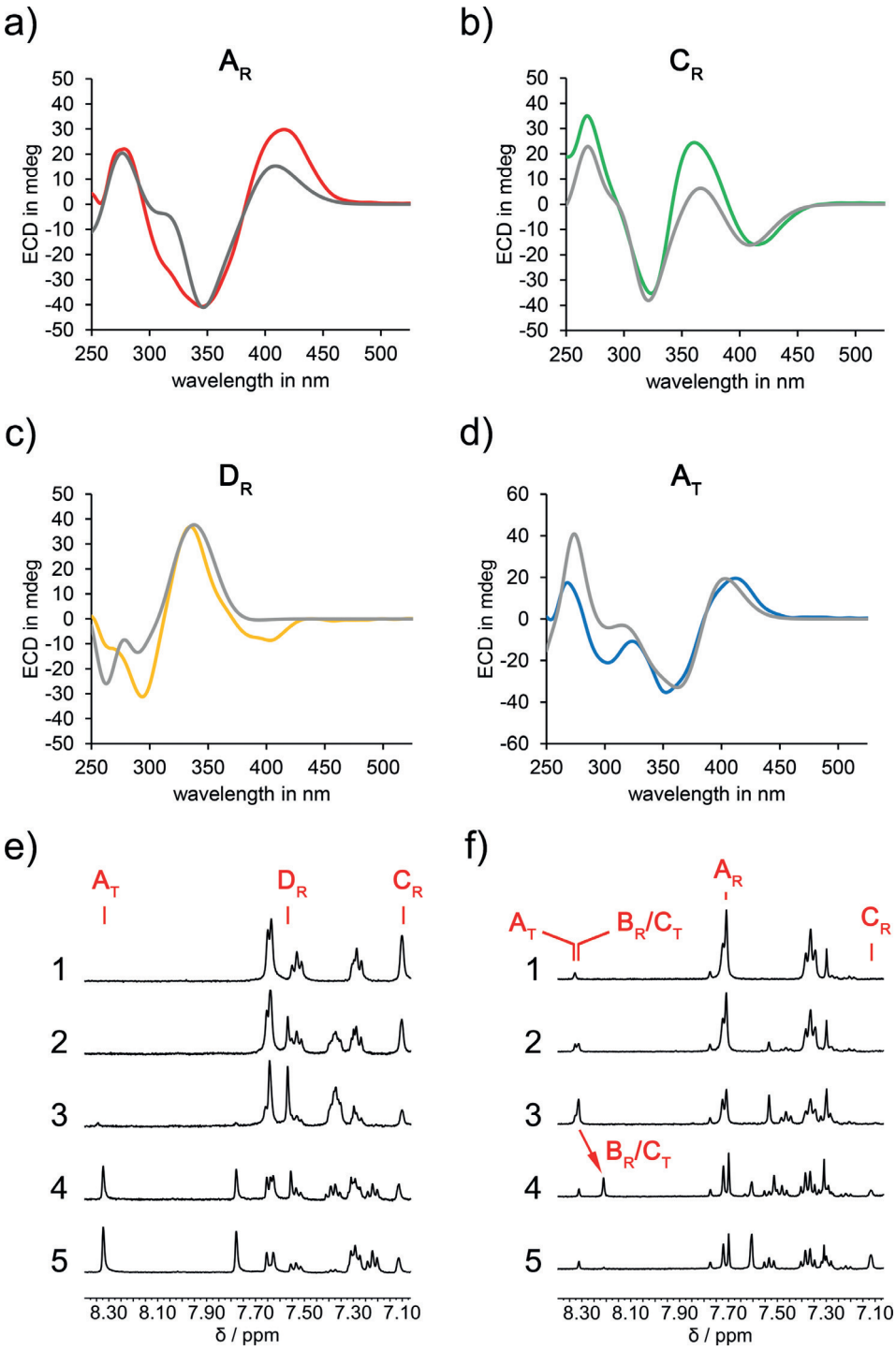

Figure 3. ECD analysis and NMR experiments showing the sequence of isomer population under irradiation conditions and at different temperatures. Experimental ECD spectra were recorded for enantiomerically pure solutions. Theoretical ECD spectra were calculated at the B3LYP-D3BJ/6–311G(d,p) level of theory. a) Experimental (red) and theoretical (gray) ECD spectra of $\mathbf{A_R}$. b) Experimental (green) and theoretical (gray) ECD spectra of $\mathbf{C_R}$. c) Experimental (orange) and theoretical (gray) ECD spectra of $\mathbf{D_R}$. d) Experimental (blue) and theoretical (gray) ECD spectra of $\mathbf{A_T}$. e) ^{1}H NMR spectra (400 MHz, CD_2Cl_2/CS_2 4:1) recorded for 1) pure $\mathbf{C_R}$ at −105 °C; 2) after 29 min of 450 nm irradiation at −105 °C; 3) after 55 min of 450 nm irradiation at −105 °C; 4) after warming to −80 °C in the dark; 5) after 23 min at −80 °C in the dark. f) ^{1}H NMR spectra (400 MHz, CD_2Cl_2/CS_2 4:1) recorded for 1) pure $\mathbf{A_R}$ at −105 °C; 2) after 5 min of 450 nm irradiation at −105 °C; 3) after 34 min of 450 nm irradiation at −105 °C; 4) after warming to −80 °C in the dark; 5) after 28 min at −80 °C in the dark.

but probably not high enough to account for the full effect. Therefore, also the transition state for $\mathbf{C_T}$ into $\mathbf{C_R}$ conversion must be significantly stabilized by the tether strain. The larger strain in $\mathbf{C_T}$ versus $\mathbf{A_T}$ can be structurally explained by the larger distance between the two phenolic oxygen atoms serving as attachment points of the linker chain in the **C** structures as opposed to the **A** structures. In the crystalline state of $\mathbf{C_R}$, the distance between these two oxygen atoms is 10.6 Å whereas in $\mathbf{A_R}$ the distance is only 7.6 Å, and a similar distance difference is seen in the theoretical description of the $\mathbf{C_T}$ and $\mathbf{A_T}$ states. This gives the linker chain greater conformational freedom in the **A** structures than in the **C** structures. Given the free activation enthalpy for the thermal conversion of $\mathbf{C_T}$ into $\mathbf{C_R}$, this process can be completely halted at −105 °C. It can thus be tested at −105 °C whether $\mathbf{C_T}$ is strongly accumulated by light irradiation of $\mathbf{A_R}$. This should be possible if 1) the energy difference between $\mathbf{B_R}$ and $\mathbf{C_T}$ is exceeding 2.0 kcal mol^{-1} prohibiting a significant thermal equilibrium between the two states and 2) $\mathbf{C_T}$ does not undergo productive photochemistry by itself. Such an accumulation was indeed observed in the analogous experiment for $\mathbf{A_T}$ when irradiating pure $\mathbf{C_R}$ at −60 °C. However, for $\mathbf{C_T}$ there is no strong accumulation possible when irradiating $\mathbf{A_R}$ at −105 °C. The most likely explanation in this case is in fact a fast thermal equilibrium between $\mathbf{C_T}$ and $\mathbf{B_R}$ enabling the establishment of a photostationary state that includes photoreactions between $\mathbf{B_R}$ and $\mathbf{A_R}$. Another indication for the presence of a significant $\mathbf{B_R}/\mathbf{C_T}$ equilibrium is the particularly strong temperature dependence of the corresponding NMR signals as opposed to

the NMR signal shifts of all other isomers (Figure 3e,f) and the ECD changes observed during irradiation of $\mathbf{A_R}$ at low temperatures (see the Supporting Information).

Taken together, the above-described measurements establish a comprehensive mechanistic picture for the six-step transmission of unidirectional rotation in **1** (Figure 2 and Figure 4). Variable-temperature experiments for selected processes further allowed us to measure the temperature dependence of ΔG between $\mathbf{C_R}$ and $\mathbf{A_R}/\mathbf{A_T}$, $\mathbf{D_R}$ and $\mathbf{A_T}$, $\mathbf{A_T}$ and $\mathbf{A_R}$, as well as of $\Delta^{\ddagger}G$ for the thermal $\mathbf{B_R}/\mathbf{C_T}$ to $\mathbf{C_R}$, $\mathbf{D_R}$ to $\mathbf{A_T}$, and $\mathbf{A_T}$ to $\mathbf{A_R}$ isomerizations (Table 1). The corresponding ΔH, ΔS, $\Delta^{\ddagger}H$, and $\Delta^{\ddagger}S$ values are reported in the Supporting Information and allow us to extrapolate free enthalpies and kinetics to different temperatures. In contrast to the usual four-step mechanism of the employed HTI motor unit, two more steps are introduced during one full 360° rotation, which represent the potential energy increase that is transmitted from the motor to the biaryl unit. In these steps, the tethered

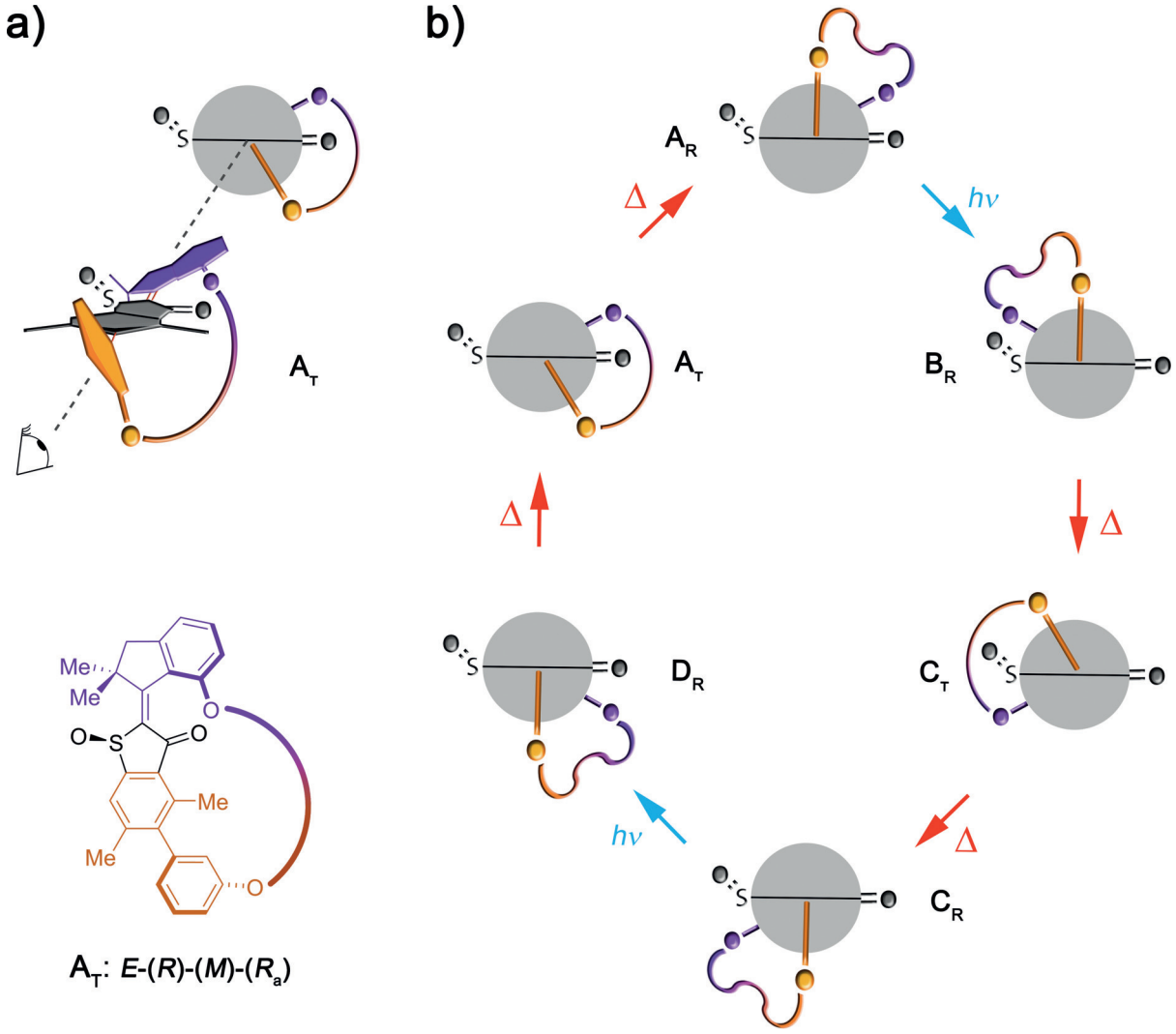

Figure 4. Stepwise unidirectional rotation of motor system **1** powered by visible-light irradiation. Only structures with *R*-configured sulfoxide stereocenter are shown for clarity. a) Schematic representation of **1** to illustrate the relative rotations of different molecular fragments. b) Six-step mechanism of the transmitted and accelerated unidirectional rotation.

Table 1: Experimental quantitative data for the operation of **1**.

$\Delta G(\mathbf{C_R}$–$\mathbf{A_R})$ [kcal mol^{-1}] (at *T*)	$\Delta G(\mathbf{D_R}$–$\mathbf{A_T})$ [kcal mol^{-1}] (at *T*)	$\Delta G(\mathbf{A_T}$–$\mathbf{A_R})$ [kcal mol^{-1}] (at *T*)	$\Delta^{\ddagger}G(\mathbf{C_R}$ to $\mathbf{A_R})$ [kcal mol^{-1}] (at *T*)	$\Delta^{\ddagger}G(\mathbf{B_R}/\mathbf{C_T}$ to $\mathbf{C_R})$ [kcal mol^{-1}] (at *T*)	$\Delta^{\ddagger}G(\mathbf{D_R}$ to $\mathbf{A_T})$ [kcal mol^{-1}] (at *T*)	$\Delta^{\ddagger}G(\mathbf{A_T}$ to $\mathbf{A_R})$ [kcal mol^{-1}] (at *T*)
1.68 (80 °C)	0.93 (−80 °C)	1.41 (0 °C)	28.41 (80 °C)	13.35 (−100 °C)	13.90 (−80 °C)	18.40 (−40 °C)
1.68 (110 °C)	0.84 (−60 °C)	1.31 (27 °C)		13.47 (−90 °C)		18.48 (−30 °C)
1.69 (140 °C)	0.75 (−40 °C)	1.30 (35 °C)		13.50 (−85 °C)		18.76 (−20 °C)
				13.62 (−80 °C)		19.15 (−5 °C)
				13.72 (−75 °C)		19.25 (0 °C)

biaryl unit is spring-loaded by the energetically downhill process of the motor's helix inversion (Figures 4b and 5). As a consequence the biaryl atropisomers are not energetically nearly degenerate anymore as it is the case for the non-tethered system **2** (Figure 5a,b; also see the Supporting Information for the determination of degeneracy). Instead, either atropisomer is energetically uplifted by the ratcheting steps of the motor unit during one full 360° rotation; 1.41 kcal mol^{-1} in $\mathbf{A_T}$ and >1.5 kcal mol^{-1} in $\mathbf{C_T}$ (Figure 5c,d; the given values correspond to 0 °C). This uplift enables >90% atropisomer interconversion in the following thermally activated steps and thus almost full rotation of the biaryl unit within one operation cycle of the machine. The change in degeneracy of the biaryl atropisomers can thus be taken as a measure for the potential energy increase—and thus the possible work—that is performed by the motor unit (Figure 5). Interestingly, the transmitted potential energy is significantly smaller than the maximum potential energy increase created in the initial photoreaction fueling the whole system when starting from $\mathbf{C_R}$. This initial potential energy increase corresponds to the energy of $\mathbf{D_R}$ and amounts to 1.97 kcal mol^{-1} (the given values were extrapolated to 0 °C). Only about 72% of that maximum possible energy are transmitted to the biaryl unit for the atropisomerization in our setup. When starting from $\mathbf{A_R}$/$\mathbf{A_T}$ more of the initial potential energy increase might be used as indicated by the complete conversion from $\mathbf{B_R}$/$\mathbf{C_T}$ into $\mathbf{C_R}$.

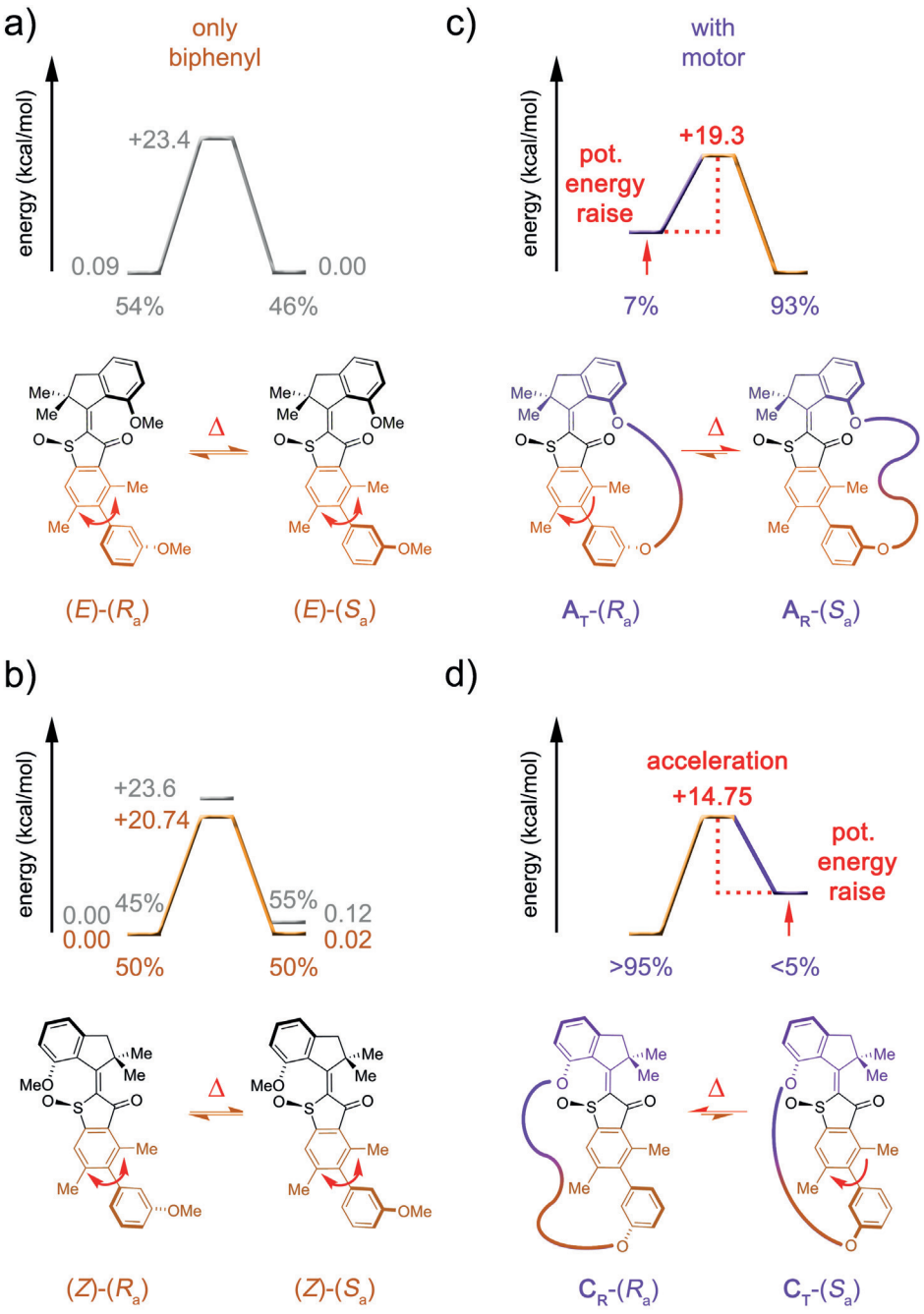

Figure 5. Rate acceleration of biaryl (orange) rotation by the molecular motor action and accompanying potential energy changes during the unidirectional 360° rotation cycle of molecular machine **1**. All values correspond to 0 °C (measured for (*Z*)-**2** and $\mathbf{A_T}$-**1**, extrapolated from variable-temperature measurements for $\mathbf{C_T}$-**1**, and calculated (gray values) for (*E*)-**2** and (*Z*)-**2**). a, b) Thermal biaryl rotation of **2** proceeds nondirectionally and encounters energy barriers in the range of 20.7 to 23.4 kcal mol^{-1}. Atropisomer energies for **2** were obtained from experiment (enantiomerically pure (*Z*)-**2**, orange values) and from the theoretical description on the B3LYP-D3BJ/6–311G(d,p) level of theory ((*E*)-**2** and (*Z*)-**2**, gray values). c, d) Action of the motor unit results in sequential and alternating increases in the biaryl atropisomer energies, enabling >90% interconversion in each case. Biaryl rotation now proceeds unidirectionally, and the associated energy barriers are lowered by up to 6.0 kcal mol^{-1}, leading to significant rate acceleration of several orders of magnitude in terms of the rate constants.

As a result of the action of the motor unit, the energy barriers for the thermal biaryl atropisomerization are significantly reduced leading to a sizeable rate enhancement for this process. To obtain the intrinsic barriers of the untethered biaryl unit, model system **2** was synthesized and experimentally scrutinized in combination with a theoretical description capturing the two transition states associated with either clockwise or counterclockwise rotation in both the *Z* and the *E* isomeric state (for details see the Supporting Information). The corresponding $\Delta^{\ddagger}G$ values

were found to be 20.74 kcal mol^{-1} for the experimentally observed atropisomerization of (*Z*)-**2** at 0 °C, which is close to the theoretical description giving 23.6 to 23.8 kcal mol^{-1} for (*Z*)-**2**, and 23.4 kcal mol^{-1} for (*E*)-**2** as shown in Figure 5. As expected, clockwise and counterclockwise atropisomerizations of **2** do not encounter significantly different energy barriers, and the energy differences between atropisomer minima are very small with $\Delta G = 0.1$ kcal mol^{-1} for both the *Z* and *E* isomers. The atropisomerization barriers are thus lowered by up to 6.0 kcal mol^{-1} ($\mathbf{C_T}$ to $\mathbf{C_R}$ transition versus (*Z*)-**2** atropisomerization; values were extrapolated to 0 °C for the former and measured at 0 °C for the latter) by the action of the molecular motor.

From these results, important design principles to increase the performance of such integrated molecular machines can be derived. It seems evident that the length of the tether connecting the motor and biaryl units provides an efficient means of changing the effectiveness of energy transmission. It is thus straightforward to assume that a more rigid or shorter tether will enable more of the potential energies of the $\mathbf{B_R}$ and $\mathbf{D_R}$ states to be harnessed by increasing the energies of the $\mathbf{A_T}$ and $\mathbf{C_T}$ states. As both the $\mathbf{B_R}$ and $\mathbf{D_R}$ states possess relaxed tethers, it is less likely that their energies would also be raised significantly by more rigid or shorter tethering. In this regard, our system behaves very differently from macrocyclic photoswitches that spring-load directly in the photoreaction.[10] In the latter cases, tether lengths and rigidities have a strong influence on the energy of the metastable switching states initially populated after the photoreaction. In our case, it is theoretically possible to increase the energies of $\mathbf{A_T}$ and $\mathbf{C_T}$ beyond the energies of the initial photoproducts $\mathbf{B_R}$ and $\mathbf{D_R}$. If the ground-state barriers between $\mathbf{B_R}$ and $\mathbf{D_R}$ and the starting states $\mathbf{A_R}$ and $\mathbf{C_R}$ remained considerably higher than all other barriers and the final states $\mathbf{A_R}$ and $\mathbf{C_R}$ still functioned as energy sinks, the initial photoreactions would still be able to power completely unidirectional rotation of the system.

Conclusion

In conclusion, we have presented a molecular machine setup enabling the transmission of the potential energy generated by a molecular motor unit onto a remote biaryl receiver moiety. As a result of the motor action, thermal atropisomerization of the biaryl is forced to proceed unidirectionally and at the same time is significantly accelerated by several orders of magnitude in terms of rate constants. Transmittance of potential energy happens during the thermally activated ratcheting steps within the rotation mechanism and were comprehensively quantified. Up to 72 % of the initial potential energy increase was found to be actually transmitted, which directly corresponds to the amount of work that the motor unit would be able to perform on the biaryl system. These findings therefore deliver a novel method for translating the power generated by a molecular motor on the nanoscale, give unprecedented insight into the working mechanism of such integrated molecular machines, and allow measuring the potential energy usable in this system. Our study thus provides a first quantitative answer to the long-standing question of how much work a single molecular motor can actually perform at the molecular scale. Finally, different isomeric states of this six-step molecular machine can be accumulated separately under different irradiation conditions, which is a highly desirable property for applications requiring multistate molecular switching. Harnessing the transmitted potential energy to actually perform work at the molecular scale will be the next big leap in this research line, and our current efforts are focused in this direction.

Acknowledgements

H.D. thanks the "Fonds der Chemischen Industrie" for a Liebig fellowship (Li 188/05) and the Deutsche Forschungsgemeinschaft (DFG) for an Emmy Noether fellowship (DU 1414/1-1). We further thank the Deutsche Forschungsgemeinschaft (SFB 749, A12) and the Cluster of Excellence "Center for Integrated Protein Science Munich" (CIPS^{M}) for financial support. We further thank Thomas Bartelmann for his help with the TOC figure and Bernhard Kempf for providing us with the "Kinetic Tools" software for data analysis.

Conflict of interest

The authors declare no conflict of interest.

Keywords: hemithioindigo · isomerization · molecular machines · photochemistry · physical chemistry

How to cite: *Angew. Chem. Int. Ed.* **2020**, *59*, 5730–5737
Angew. Chem. **2020**, *132*, 5779–5786

[1] a) N. Koumura, R. W. J. Zijlstra, R. A. van Delden, B. L. Feringa, *Nature* **1999**, *401*, 152–155; b) S. P. Fletcher, F. Dumur, M. M. Pollard, B. L. Feringa, *Science* **2005**, *310*, 80–82; c) J. V. Hernandez, E. R. Kay, D. A. Leigh, *Science* **2004**, *306*, 1532–1537; d) M. J. Barrell, A. G. Campana, M. von Delius, E. M. Geertsema, D. A. Leigh, *Angew. Chem. Int. Ed.* **2011**, *50*, 285–290; *Angew. Chem.* **2011**, *123*, 299–304; e) L. Greb, J. M. Lehn, *J. Am. Chem. Soc.* **2014**, *136*, 13114–13117; f) L. Greb, A. Eichhofer, J. M. Lehn, *Angew. Chem. Int. Ed.* **2015**, *54*, 14345–14348; *Angew. Chem.* **2015**, *127*, 14553–14556; g) S. Kassem, T. van Leeuwen, A. S. Lubbe, M. R. Wilson, B. L. Feringa, D. A. Leigh, *Chem. Soc. Rev.* **2017**, *46*, 2592–2621; h) S. Erbas-Cakmak, S. D. P. Fielden, U. Karaca, D. A. Leigh, C. T. McTernan, D. J. Tetlow, M. R. Wilson, *Science* **2017**, *358*, 340–343; i) M. R. Wilson, J. Sola, A. Carlone, S. M. Goldup, N. Lebrasseur, D. A. Leigh, *Nature* **2016**, *534*, 235–240; j) M. Guentner, M. Schildhauer, S. Thumser, P. Mayer, D. Stephenson, P. J. Mayer, H. Dube, *Nat. Commun.* **2015**, *6*, 8406; k) L. A. Huber, K. Hoffmann, S. Thumser, N. Böcher, P. Mayer, H. Dube, *Angew. Chem. Int. Ed.* **2017**, *56*, 14536–14539; *Angew. Chem.* **2017**, *129*, 14728–14731; l) R. Wilcken, M. Schildhauer, F. Rott, L. A. Huber, M. Guentner, S. Thumser, K. Hoffmann, S. Oesterling, R. de Vivie-Riedle, E. Riedle, H. Dube, *J. Am. Chem. Soc.* **2018**, *140*, 5311–5318; m) M. Schildhauer, F. Rott, S. Thumser, P. Mayer, R. de Vivie-Riedle, H. Dube, *ChemPhotoChem* **2019**, *3*, 365–371; n) D. Roke, M. Sen, W. Danowski, S. J. Wezenberg,

B. L. Feringa, *J. Am. Chem. Soc.* **2019**, *141*, 7622 – 7627; o) B. S. L. Collins, J. C. M. Kistemaker, E. Otten, B. L. Feringa, *Nat. Chem.* **2016**, *8*, 860 – 866; p) R. D. Astumian, *Acc. Chem. Res.* **2018**, *51*, 2653 – 2661.

[2] a) E. R. Kay, D. A. Leigh, F. Zerbetto, *Angew. Chem. Int. Ed.* **2007**, *46*, 72 – 191; *Angew. Chem.* **2007**, *119*, 72 – 196; b) S. Erbas-Cakmak, D. A. Leigh, C. T. McTernan, A. L. Nussbaumer, *Chem. Rev.* **2015**, *115*, 10081 – 10206; c) G. Ragazzon, M. Baroncini, S. Silvi, M. Venturi, A. Credi, *Nat. Nanotechnol.* **2015**, *10*, 70 – 75; d) M. Baroncini, L. Casimiro, C. de Vet, J. Groppi, S. Silvi, A. Credi, *ChemistryOpen* **2018**, *7*, 169 – 179; e) M. Baroncini, S. Silvi, A. Credi, *Chem. Rev.* **2020**, *120*, 200 – 268.

[3] a) E. Uhl, S. Thumser, P. Mayer, H. Dube, *Angew. Chem. Int. Ed.* **2018**, *57*, 11064 – 11068; *Angew. Chem.* **2018**, *130*, 11231 – 11235; b) P. Štacko, J. C. M. Kistemaker, T. van Leeuwen, M.-C. Chang, E. Otten, B. L. Feringa, *Science* **2017**, *356*, 964 – 968; c) S. F. Pizzolato, P. Stacko, J. C. M. Kistemaker, T. van Leeuwen, E. Otten, B. L. Feringa, *J. Am. Chem. Soc.* **2018**, *140*, 17278 – 17289.

[4] a) Q. Li, G. Fuks, E. Moulin, M. Maaloum, M. Rawiso, I. Kulic, J. T. Foy, N. Giuseppone, *Nat. Nanotechnol.* **2015**, *10*, 161 – 165; b) J. T. Foy, Q. Li, A. Goujon, J.-R. Colard-Itte, G. Fuks, E. Moulin, O. Schiffmann, D. Dattler, D. P. Funeriu, N. Giuseppone, *Nat. Nanotechnol.* **2017**, *12*, 540 – 545; c) J. Chen, F. K. Leung, M. C. A. Stuart, T. Kajitani, T. Fukushima, E. van der Giessen, B. L. Feringa, *Nat. Chem.* **2018**, *10*, 132 – 138; d) R. Eelkema, M. M. Pollard, J. Vicario, N. Katsonis, B. S. Ramon, C. W. Bastiaansen, D. J. Broer, B. L. Feringa, *Nature* **2006**, *440*, 163; e) W. R. Browne, B. L. Feringa, *Nat. Nanotechnol.* **2006**, *1*, 25 – 35.

[5] a) A. Coskun, M. Banaszak, R. D. Astumian, J. F. Stoddart, B. A. Grzybowski, *Chem. Soc. Rev.* **2012**, *41*, 19 – 30; b) C. Pezzato, C. Cheng, J. F. Stoddart, R. D. Astumian, *Chem. Soc. Rev.* **2017**, *46*, 5491 – 5507.

[6] E. Uhl, P. Mayer, H. Dube, *ChemRxiv* **2019**, https://doi.org/10.26434/chemrxiv.10048871.v10048871.

[7] a) P. Friedländer, *Ber. Dtsch. Chem. Ges.* **1906**, *39*, 1060 – 1066; b) S. Wiedbrauk, H. Dube, *Tetrahedron Lett.* **2015**, *56*, 4266 – 4274; c) V. A. Izmail'skii, M. A. Mostoslavskii, *Ukr. Khem. Zh.* **1961**, *27*, 234 – 237.

[8] C. Petermayer, H. Dube, *Acc. Chem. Res.* **2018**, *51*, 1153 – 1163.

[9] a) K. Tanaka, K. Kohayakawa, S. Iwata, T. Irie, *J. Org. Chem.* **2008**, *73*, 3768 – 3774; b) T. Lougheed, V. Borisenko, T. Hennig, K. Rück-Braun, G. A. Woolley, *Org. Biomol. Chem.* **2004**, *2*, 2798 – 2801; c) S. Herre, T. Schadendorf, I. Ivanov, C. Herrberger, W. Steinle, K. Rück-Braun, R. Preissner, H. Kuhn, *ChemBioChem* **2006**, *7*, 1089 – 1095; d) S. Kitzig, M. Thilemann, T. Cordes, K. Rück-Braun, *ChemPhysChem* **2016**, *17*, 1252 – 1263; e) K. Eggers, T. M. Fyles, P. J. Montoya-Pelaez, *J. Org. Chem.* **2001**, *66*, 2966 – 2977; f) M. Guentner, E. Uhl, P. Mayer, H. Dube, *Chem. Eur. J.* **2016**, *22*, 16433 – 16436; g) S. Wiedbrauk, T. Bartelmann, S. Thumser, P. Mayer, H. Dube, *Nat. Commun.* **2018**, *9*, 1456; h) K. Hoffmann, M. Guentner, P. Mayer, H. Dube, *Org. Chem. Front.* **2019**, *6*, 1244 – 1252; i) F. Kink, M. P. Collado, S. Wiedbrauk, P. Mayer, H. Dube, *Chem. Eur. J.* **2017**, *23*, 6237 – 6243; j) A. Sailer, F. Ermer, Y. Kraus, F. H. Lutter, C. Donau, M. Bremerich, J. Ahlfeld, O. Thorn-Seshold, *ChemBioChem* **2019**, *20*, 1305 – 1314.

[10] a) Q. Li, H. Qian, B. Shao, R. P. Hughes, I. Aprahamian, *J. Am. Chem. Soc.* **2018**, *140*, 11829 – 11835; b) Z. Huang, R. Boulatov, *Chem. Soc. Rev.* **2011**, *40*, 2359 – 2384; c) Q. Z. Yang, Z. Huang, T. J. Kucharski, D. Khvostichenko, J. Chen, R. Boulatov, *Nat. Nanotechnol.* **2009**, *4*, 302 – 306; d) C. L. Sun, C. Wang, R. Boulatov, *ChemPhotoChem* **2019**, *3*, 268 – 283.

[11] CCDC 1962416 (**2**), 1943797 ($\mathbf{A_R}$-**1**), and 1943796 ($\mathbf{C_R}$-**1**) contain the supplementary crystallographic data for this paper. These data are provided free of charge by The Cambridge Crystallographic Data Centre.

Manuscript received: October 29, 2019
Revised manuscript received: December 9, 2019
Accepted manuscript online: January 15, 2020
Version of record online: February 20, 2020

